Phase Distribution, Composition and Disorder in $Y_2(Hf,Sn)_2O_7$ Ceramics: Insights from Solid-State NMR Spectroscopy and First-Principles Calculations

Robert F. Moran,[1] Arantxa Fernandes,[1] Daniel M. Dawson,[1] Scott Sneddon,[1] Amy S. Gandy,[2] Nik Reeves-McLaren,[2] Karl R. Whittle[2,3] and Sharon E. Ashbrook,[1]*

[1]*School of Chemistry, EaStCHEM and Centre of Magnetic Resonance, University of St Andrews, St Andrews KY16 9ST, United Kingdom*

[2]*Department of Materials Science and Engineering, University of Sheffield, Mappin Street, Sheffield S1 3JD, UK*

[3]*School of Engineering, University of Liverpool, Brownlow Hill, Liverpool, L69 3GH, UK*

Supporting Information

S1. Powder X-ray diffraction measurements

Figure S1.1 shows powder X-ray diffraction (pXRD) measurements for $Y_2Hf_{2-x}Sn_xO_7$, indicating no significant impurities are seen by diffraction.

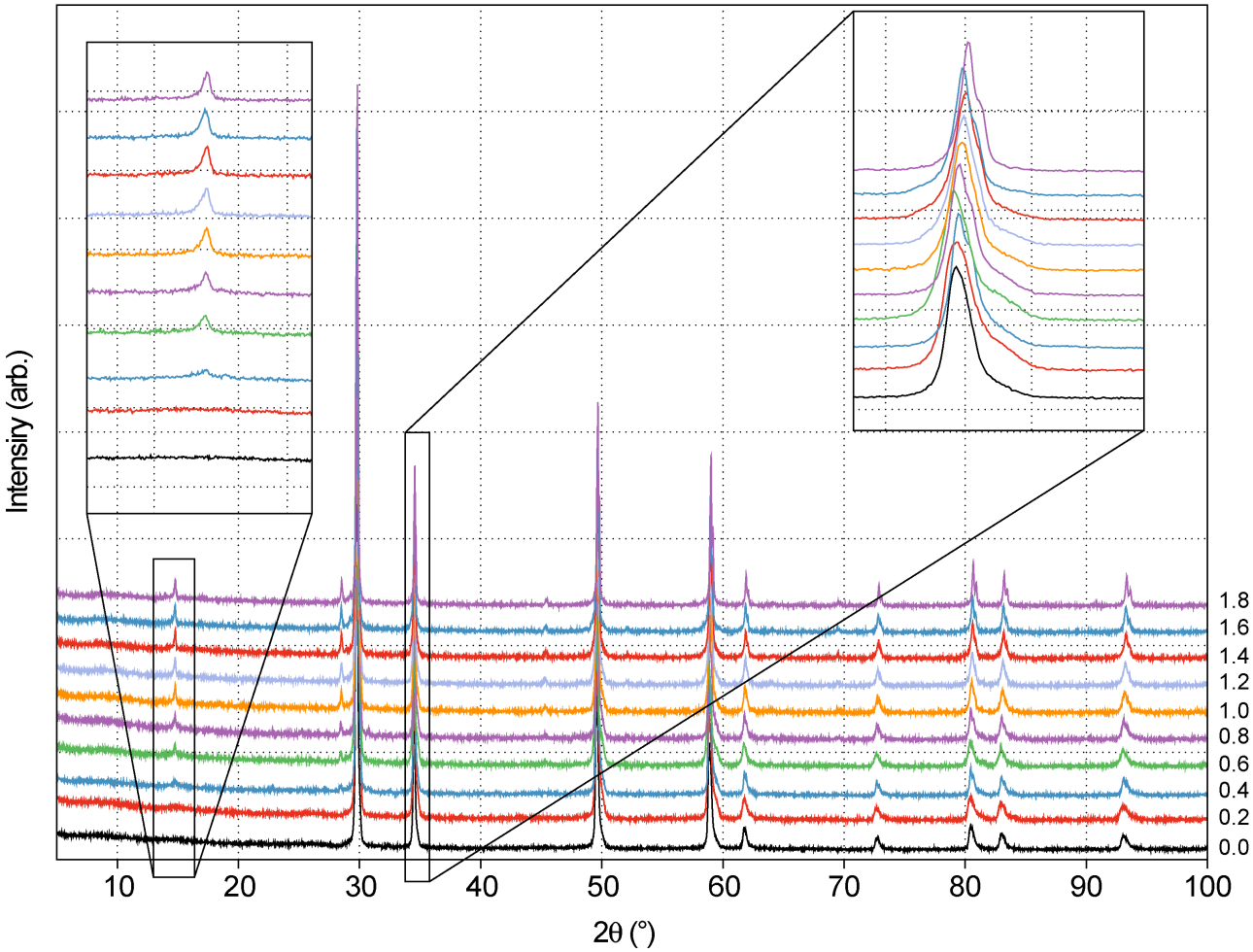

Figure S1.1. Powder XRD patterns for $Y_2Hf_{2-x}Sn_xO_7$.

S2. Further information on DFT calculations

Calculations of total energies and NMR parameters were carried out using the CASTEP density functional theory (DFT) code (version 8.0),[S1-S2] employing the gauge-including projector augmented wave (GIPAW) approach[S1] to reconstruct the all-electron wavefunction in the presence of a magnetic field. Calculations were performed using the GGA PBE functional[S3] and core-valence interactions were described by ultrasoft pseudopotentials,[S4] accounting for scalar relativistic effects using ZORA.[S5] A planewave energy cutoff of 60 Ry (~816 eV) was used, and integrals over the first Brillouin zone were performed using a Monkhorst-Pack grid[S6] with a k-point spacing of 0.04 2π Å^{-1}. All calculations were converged as far as possible with respect to both k-point spacing and energy cutoff. In the geometry optimisation all atomic coordinates and unit cell parameters were allowed to vary, with a geometry optimization energy tolerance of 1×10^{-5} eV per atom and an electronic structure energy tolerance of 1×10^{-9} eV per atom used.

Referencing

To facilitate comparison to experiment σ_{iso}^{calc} values were converted to δ_{iso}^{calc} values. For ^{89}Y, this was achieved by comparing experimental and calculated NMR parameters for a series of simple yttrium-containing solids, as described in Ref. S7. From the line of best fit, shown in Figure S2.1 it can be seen that

$$\delta_{iso}^{calc} = -0.9864\, \sigma_{iso}^{calc} + 2652.5547 \ . \qquad \text{(S2.1)}$$

as described in Ref. S7 and shown in Figure S2.1. A ^{119}Sn reference shielding was determined by comparing the experimental shift of $Y_2Sn_2O_7$ ($\delta_{iso}^{exp} = -582$ ppm[S8]) and calculated shielding ($\sigma_{iso}^{calc} = 3183.94$ ppm), giving $\sigma_{ref} = 2601.94$ ppm. δ_{iso}^{calc} is then given by

$$\delta_{iso}^{calc} = \sigma_{iso}^{calc} - \sigma_{ref} \ . \qquad \text{(S2.2)}$$

For ^{17}O, an approach similar to that outlined in Ref. S9 was used (with the inclusion of one additional oxide (BaO), where experimental and calculated NMR parameters for a series of oxides were compared. The line of best fit,

$$\delta_{iso}^{calc} = -0.9002\,\sigma_{iso}^{calc} + 228.8128\ , \qquad \text{(S2.3)}$$

is shown in Figure S2.2. Note that previous calculations were carried out with slightly lower cut off energies and k points, but as these are well converged any uncertainty in the reference shielding is estimated to e less than 1% of the shift range.

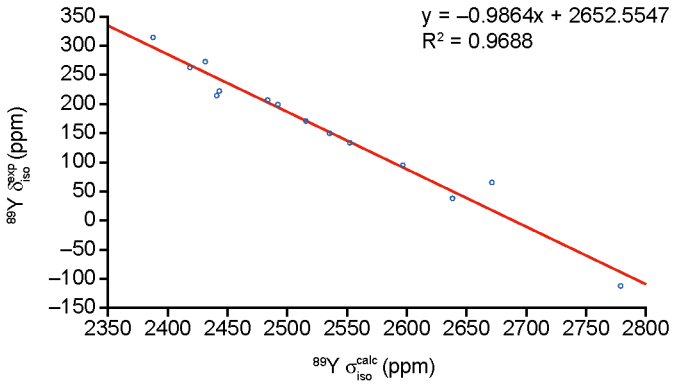

Figure S2.1. Plot of ^{89}Y experimental δ_{iso} against calculated σ_{iso} for a series of yttrium-containing compounds.[S7]

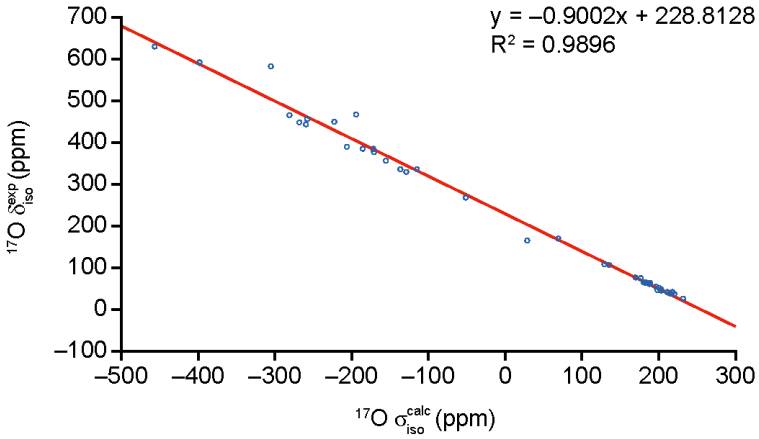

Figure S2.2. Plot of ^{17}O experimental δ_{iso} against calculated σ_{iso} for a series of oxides.[S9]

Pyrochlore models

Calculations were performed for a single unit cell of $Y_2Sn_2O_7$, where the environment of one of the Y or Sn species was modified systematically, altering both the number of the surrounding B-site cations (*i.e.*, Sn and Hf) and their spatial arrangement, as shown in Figure S2.3. In each case, the geometry of the structure was optimized (with atomic coordinates and unit cell parameters allowed to vary), prior to calculation of the NMR parameters. A similar set of calculations was performed for a hypothetical $Y_2Hf_2O_7$ pyrochlore, to enable the prediction of chemical shifts resulting from environments with a greater proportion of Hf in either the NNN or long-range environment. For the Sn centered calculations a single Sn was first placed into the $Y_2Hf_2O_7$ structure and its environment then modified as described above. This approach generated a total of 52 structural models (26 Y centered and 26 Sn centered). A further two models were created by moving firstly one, and subsequently two, 8a O species in $Y_2Sn_2O_7$ to vacant 8b sites surrounding Sn, thereby creating seven- and eight-coordinated Sn respectively. ^{119}Sn chemical shifts predicted for these models are shown in Figure 6b of the main text. Figure S2.3 shows the local atomic environments around the pyrochlore A and B sites, and the numbering scheme used to denote the different arrangements of the atoms on the six next nearest neighbour (NNN) B sites in each case.

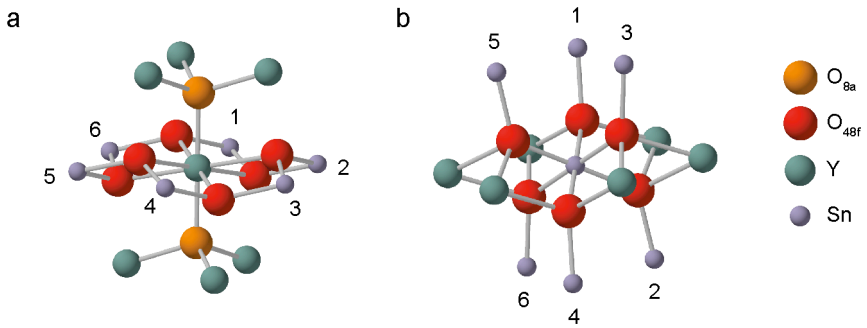

Figure S2.3. The local environment around the pyrochlore (a) A site (occupied by Y) and (b) B site (occupied by Sn or Hf), showing the numbering scheme used.

Defect fluorite models

A set of 30 $Y_2Hf_2O_7$ defect fluorite structural models was produced, starting from a $2 \times 2 \times 2$ supercell of ideal AO_2 fluorite, as described in Ref. S9. 16 of the 32 cation sites were

randomly selected to be occupied by Y, with the remainder occupied by Hf. Similarly, 8 of the 64 anion sites were randomly selected to be vacant (and the remaining 56 occupied by O). The structures were optimised using DFT. In addition, a further four structural models were considered. The first was a $Y_2Hf_2O_7$ pyrochlore structure (*i.e.*, with ordering of cations and anions) generated by atom substitution from a structural model of $Y_2Sn_2O_7$. Two models were generated from this; one by moving one 8a O to a vacant 8b site (creating a seven-coordinate Y species and an OHf_4 environment), and a second by moving another 8a O from around the same Y to a vacant 8b site (creating a six-coordinate Y species). The final structural model was a reverse pyrochlore structure, *i.e.*, containing Y on the B site and Hf on the A site. All structures were optimised. In order to gain insight into the chemical shift changes seen upon Sn substitution into $Y_2Hf_2O_7$, the lowest energy structure from the 34 $Y_2Hf_2O_7$ models discussed above was used. Distinct OY3Hf, OY2Hf2, OYHf3 and OHf4 species were manually modified by substituting a six-coordinate Hf^{4+} cation with a Sn^{4+} (as Sn has been shown to prefer to be six coordinate in this work and in previous studies) to give four separate new structural models.

Calculated shift anisotropies

Figure S2.4 shows a plot of the variation in the calculated ^{89}Y Ω for the 26 Y-centred pyrochlore models of $Y_2(Hf,Sn)_2O_7$ as the number n of Sn NNN varies. An increase in the average Ω of ~90 ppm with each Hf added is observed.

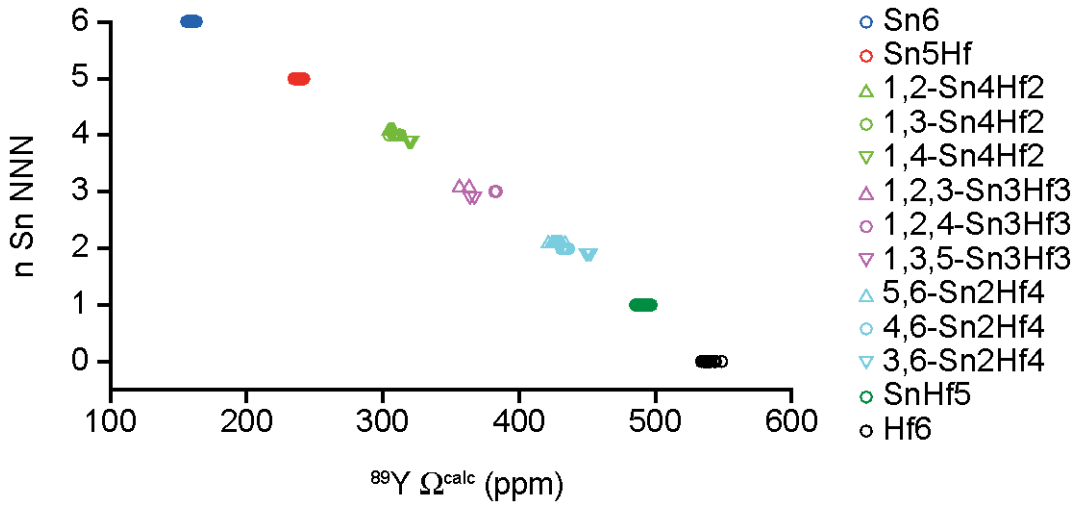

Figure S2.4. Plot showing calculated (using DFT) ^{89}Y Ω for the 26 Y-centred pyrochlore models of $Y_2(Hf,Sn)_2O_7$ with respect to the number n of Sn NNN.

Figure S2.5 shows a plot of the variation in the calculated ^{119}Sn Ω for the 26 Sn-centred pyrochlore models of $Y_2(Hf,Sn)_2O_7$ as the number n of Sn NNN varies.

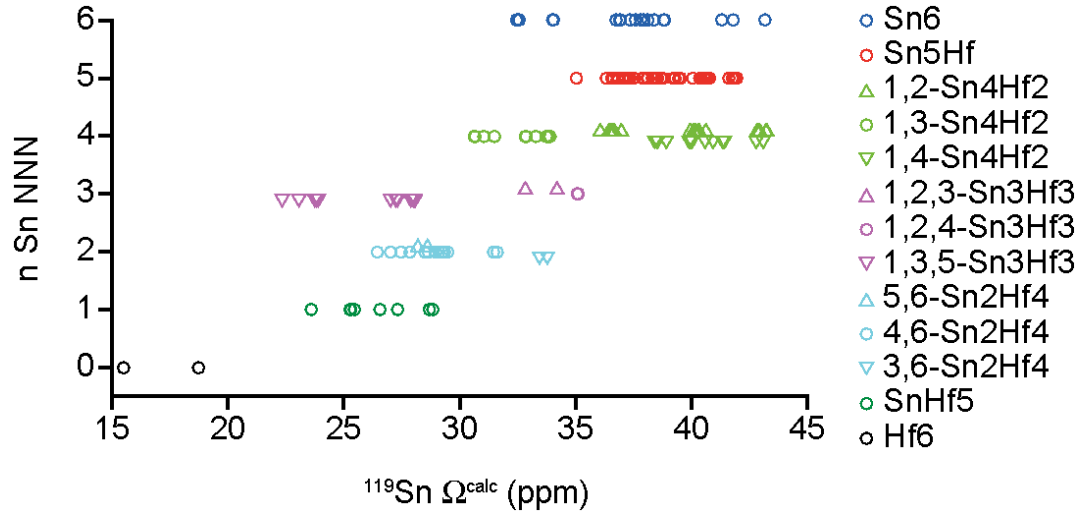

Figure S2.5. Plot showing calculated (using DFT) ^{119}Sn Ω for the 26 Sn-centred pyrochlore models of $Y_2(Hf,Sn)_2O_7$ with respect to the number n of Sn NNN.

^{17}O DFT calculations

Figure S2.6 shows calculated ^{17}O δ_{iso}^{calc} for O1 (OY4) environments in pyrochlore models of $Y_2Sn_2O_7$ and $Y_2Sn_2O_7$ substituted with 1 and 2 Hf, plotted as a function of the number of Hf species on the next next nearest neighbouring (NNNN) B sites (*i.e.*, O-Y-O-Hf linkages).

Calculations predict a small (~0.3 ppm) decrease in δ_{iso}^{calc} with increasing numbers of Hf substituted onto the B sites.

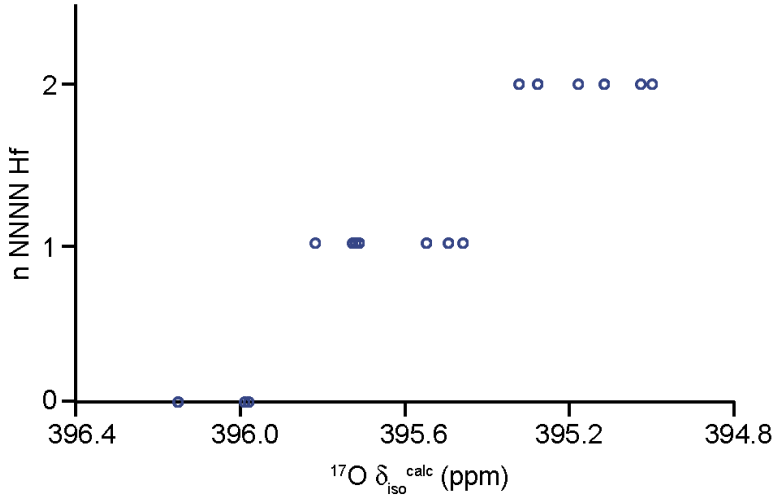

Figure S2.6. Plot showing calculated ^{17}O δ_{iso} for O1 (OY4) environments (with n Hf NNNN) in pyrochlore models of $Y_2Sn_2O_7$ and $Y_2Sn_2O_7$ substituted with one or two Hf.

Figure S2.7 shows how the calculated ^{17}O C_Q for pyrochlore models of $Y_2(Hf,Sn)_2O_7$ varies with the distortion index. The distortion index is a measure of the deviation from ideal tetrahedral coordination environment, and is given by

$$DI = \frac{\sum_i |\theta_i - \theta_0|}{6}, \qquad \text{(S2.1)}$$

where θ_0 is the ideal tetrahedral angle (109.471°). The plot shows that the variation in calculated C_Q observed between OY2Hf2, OY2Sn2 and OY2Hf2 environments does not arise from increased distortion in the local environment. This difference likely arises from the increased covalency of the Sn-O bond (in comparison to Hf-O and Y-O) that results in more directional bonding and a decrease in the symmetry of the local environment.

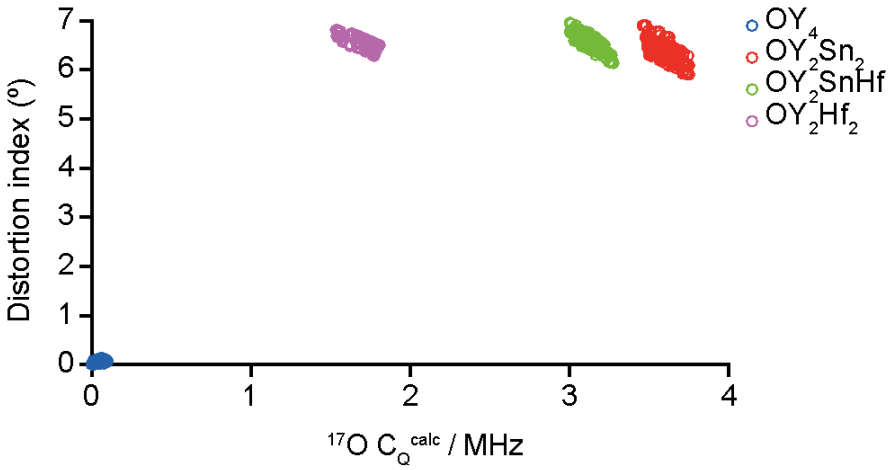

Figure S2.7. Plot showing the variation of calculated ^{17}O C_Q for pyrochlore models of $Y_2(Hf,Sn)_2O_7$ with distortion index.

S3. CSA-amplified PASS experiments

^{89}Y and ^{119}Sn two-dimensional CSA-amplified PASS NMR experiments were carried out using the pulse sequence of Orr *et al.*[S10-S11] For ^{89}Y NMR experiments, the original pulse sequence was modified to include an initial saturation train. The total scaling factor is given by $\chi_T = (n_{PASS} + 1)\ \chi$, where χ is the scaling factor (determined by the timing of the five π pulse blocks) and n_{PASS} is the number of additional blocks used. Cogwheel phase cycling[S12] was used in order to reduce the length of the phase cycle required. Fitting of the sideband manifold extracted from the indirect dimension of the two-dimensional CSA-amplified PASS spectrum was carried out using SIMPSON[S13] by comparison to a simulated two-dimensional CSA-amplified PASS experiment using ideal pulses for ^{119}Sn, and simulating the complete two-dimensional NMR experiment using an estimated radiofrequency field strength for ^{89}Y. The 'root mean square' (rms) error quoted in tables and plotted in figures is that outputted by SIMPSON and described in Ref. S13.

Table S3.1 gives the acquisition parameters used for ^{89}Y and ^{119}Sn two-dimensional CSA-amplified PASS NMR spectra.

Table S3.1. Acquisition parameters for ^{89}Y and ^{119}Sn two-dimensional CSA-amplified PASS experiments.

Parameter	^{89}Y	^{119}Sn
B_0 / T	14.1	9.4
MAS rate in F_1 / kHz	1.5	1.87
MAS rate in F_2 / kHz	10.0	14.0
Spectral width / kHz	24.0	29.9
Number of rows	16	16
χ_T	6.6667	7.5
χ	3.3333	2.5
n_{PASS}	2	3
Number of transients	962 – 4498	76
Recycle interval / s	10	30
Saturation delay / ms	50	
Number of saturation pulses	16	

^{89}Y CSA parameters were measured using two-dimensional CSA-amplified PASS experiments for $Y_2Hf_{2-x}Sn_xO_7$ samples with x = 2.0 to 1.0. The values extracted, along with the corresponding rms error for the fits, are given in Table S3.2. As an example, Figure S3.1 shows the ^{89}Y two-dimensional CSA-amplified PASS spectrum of $Y_2Hf_{0.4}Sn_{1.6}O_7$. Also shown are analytical fits (fitted by simulating the complete two-dimensional NMR experiment using an estimated radiofrequency field strength for ^{89}Y) and the plots of the rms error for the three spinning sideband manifolds.

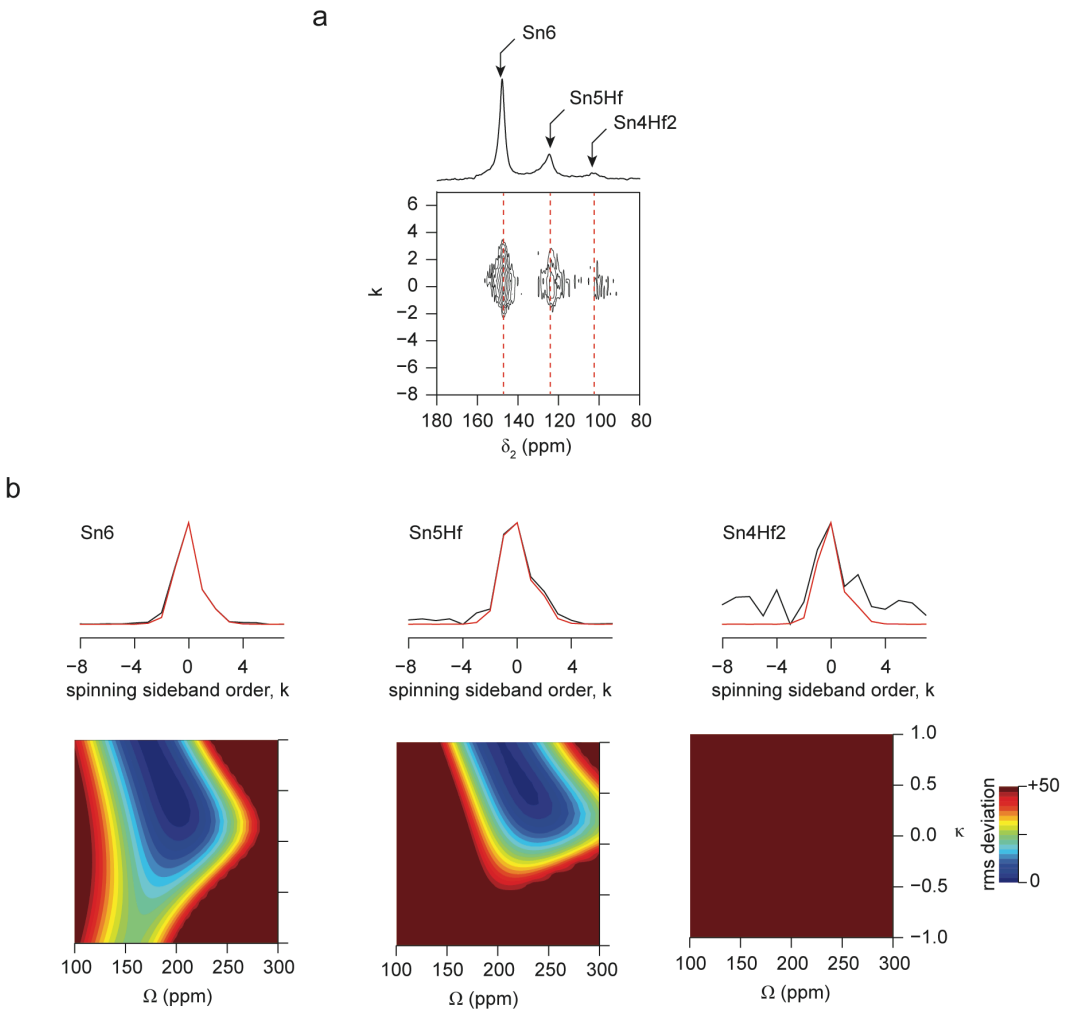

Figure S3.1 (a) ^{89}Y (14.1 T) two-dimensional CSA-amplified PASS spectrum of $Y_2Hf_{0.4}Sn_{1.6}O_7$. See Table S3.1 for experimental acquisition parameters. (b) Extracted spinning sideband manifolds for the three resonances along with their corresponding analytical fits, shown in red. Also shown are the contour plots of rms error (arbitrarily restricted from 0 to 50).

Table S3.2. Experimental ^{89}Y NMR parameters (Ω and κ) and corresponding rms error resulting from the analytical fits of the spinning sideband manifolds of the pyrochlore peaks extracted from the two-dimensional CSA-amplified PASS spectra of $Y_2Hf_{2-x}Sn_xO_7$.

Compound	δ_{iso} (ppm)[a]	Ω (ppm)	κ	rms error	NNN
$Y_2Sn_2O_7$	147.9	209 ± 13	0.5 ± 0.3	0.5	Sn6
$Y_2Hf_{0.2}Sn_{1.8}O_7$	147.9	210 ± 13	0.5 ± 0.3	0.5	Sn6
	124.9	256 ± 12	0.2 ± 0.1	9.7	Sn5Hf
	103.3				Sn4Hf2
$Y_2Hf_{0.4}Sn_{1.6}O_7$	147.9	203 ± 17	0.5 ± 0.3	0.6	Sn6
	125.2	234 ± 19	0.7 ± 0.2	1.6	Sn5Hf
	102.9				Sn4Hf2
$Y_2Hf_{0.6}Sn_{1.4}O_7$	147.9	206 ± 19	0.6 ± 0.3	0.5	Sn6
	125.1	234 ± 17	0.8 ± 0.2	5.3	Sn5Hf
	103.2	244 ± 13	0.8 ± 0.1	59.4	Sn4Hf2
$Y_2Hf_{0.8}Sn_{1.2}O_7$	147.9	198 ± 19	0.7 ± 0.3	0.8	Sn6
	125.3	227 ± 17	1.0 ± 0.2	3.1	Sn5Hf
	103.4	275 ± 13	0.8 ± 0.1	30.9	Sn4Hf2
Y_2HfSnO_7	148.9	193 ± 22	0.9 ± 0.3	1.2	Sn6
	125.5	249 ± 12	0.6 ± 0.2	7.5	Sn5Hf
	103.8	260 ± 14	0.7 ± 0.2	32.1	Sn4Hf2

[a] Errors in δ_{iso} are estimated to be ± 0.5 ppm.

^{119}Sn CSA parameters were measured using two-dimensional CSA-amplified PASS experiments for $Y_2Hf_{2-x}Sn_xO_7$ samples with x = 2.0 to 1.0. The values extracted, along with the corresponding rms error for the fits, are given in Table S3.3. As an example, Figure S3.2 shows the ^{119}Sn two-dimensional CSA-amplified PASS spectrum of $Y_2Hf_{0.4}Sn_{1.6}O_7$. Also shown are analytical fits (fitted by comparison to a simulated two-dimensional CSA-amplified PASS experiment using ideal pulses) and the plots of the rms error for the three spinning sideband manifolds.

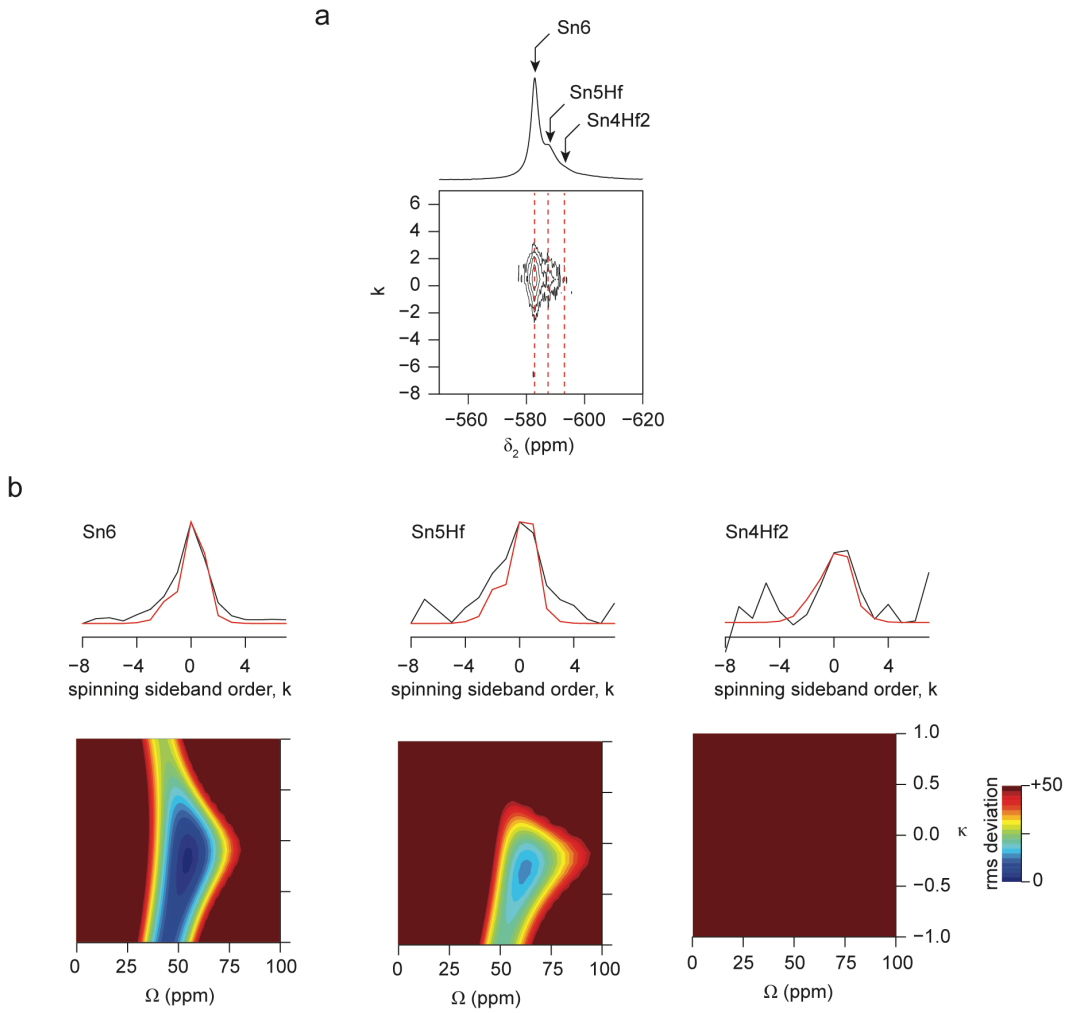

Figure S3.2 (a) ^{119}Sn (9.4 T) two-dimensional CSA-amplified PASS spectrum of $Y_2Hf_{0.4}Sn_{1.6}O_7$. See Table S3.1 for experimental acquisition parameters. (b) Extracted spinning sideband manifolds for the three resonances along with their corresponding analytical fits, shown in red. Also shown are the contour plots of rms error (arbitrarily restricted from 0 to 50).

Table S3.3. Experimental ^{119}Sn NMR parameters (Ω and κ) and corresponding rms error resulting from the analytical fits of the spinning sideband manifolds of the pyrochlore peaks extracted from the two-dimensional CSA-amplified PASS spectra of $Y_2Hf_{2-x}Sn_xO_7$.

Compound	δ_{iso} (ppm)[a]	Ω (ppm)	κ	rms error	NNN
$Y_2Sn_2O_7$	−582.6	43 ± 5	−1.0 ± 0.1		Sn6
$Y_2Hf_{0.2}Sn_{1.8}O_7$	−582.7	44 ± 3	−1.0 ± 0.2	4.7	Sn6
	−587.8	36 ± 4	−1.0 ± 0.4	25.0	Sn5Hf
$Y_2Hf_{0.4}Sn_{1.6}O_7$	−582.8	46 ± 3	−1.0 ± 0.2	7.7	Sn6
	−587.8	52 ± 4	−1.0 ± 0.2	20.0	Sn5Hf
	−593.1	62 ± 4	−0.3 ± 0.4	62.7	Sn4Hf2
$Y_2Hf_{0.6}Sn_{1.4}O_7$	−582.7	43 ± 3	−1.0 ± 0.2	1.2	Sn6
	−587.8	44 ± 3	−1.0 ± 0.2	7.5	Sn5Hf
	−592.9[b]				Sn4Hf2

[a] Errors in δ_{iso} are estimated to be ± 0.5 ppm.

[b] The intensity of this resonance is too low to extract the spinning sideband manifold.

S4. Further information on ^{89}Y MAS NMR spectra

Figure S4.1 shows the effect of including the broad resonances associated with the presence of a defect fluorite phase in the analytical fitting of ^{89}Y MAS NMR spectra of $Y_2Hf_{0.2}Sn_{1.8}O_7$.

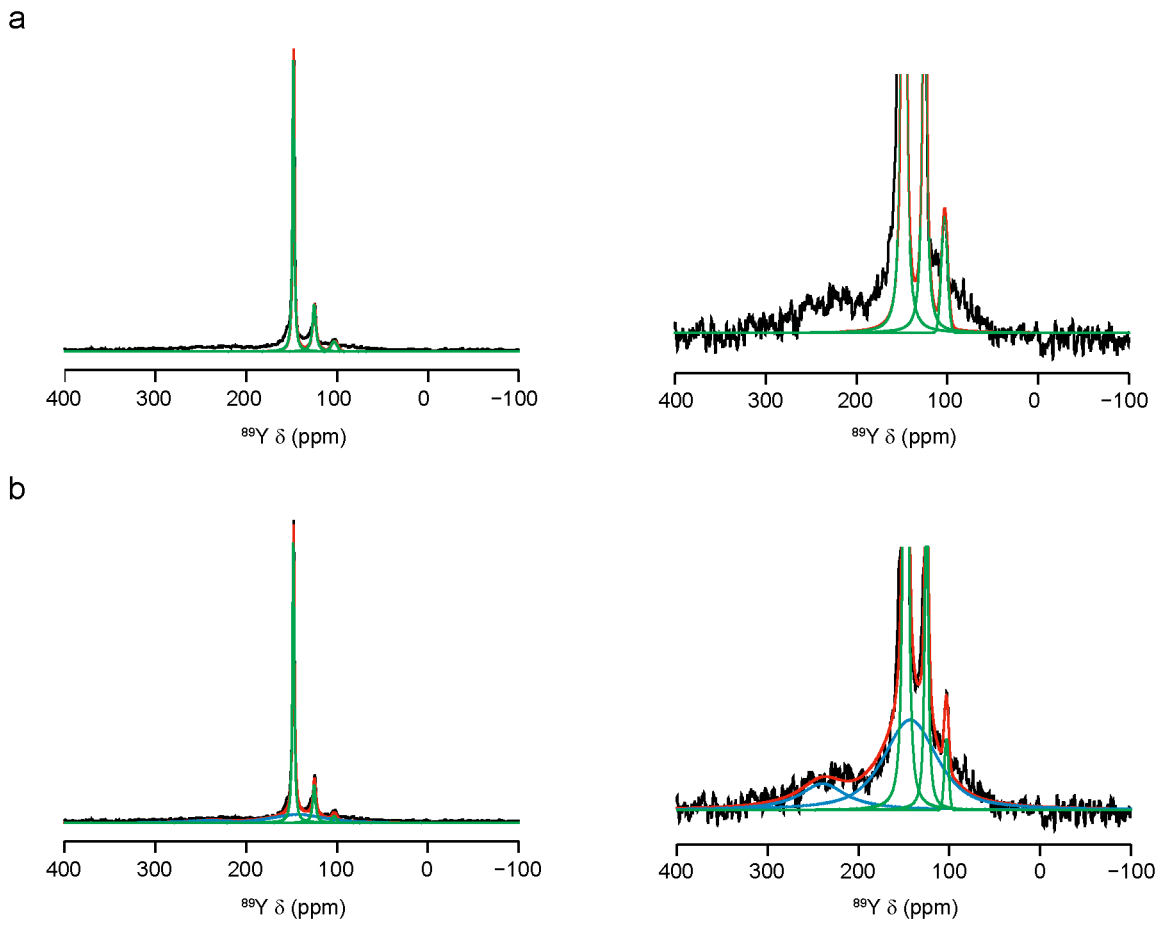

Figure S4.1. Analytical fits and corresponding (vertical) expansions of the ^{89}Y MAS NMR spectrum of $Y_2Hf_{0.2}Sn_{1.8}O_7$. In (a), the spectrum is fitted without the inclusion of the broad resonances associated with the disordered defect fluorite phase. In (b), two broad resonances are included. The green, blue and red lines denote the analytical fit for the pyrochlore phase, defect fluorite phase and all resonances, respectively.

From a fitting of each of the ^{89}Y MAS NMR spectra of $Y_2Hf_{2-x}Sn_xO_7$ in Figure 2 of the main text, the chemical shifts of the individual components, and their relative intensities can be

extracted. These are given in Table 1 (main text) and shown in Figure S4.2 as a function of the composition of the starting materials.

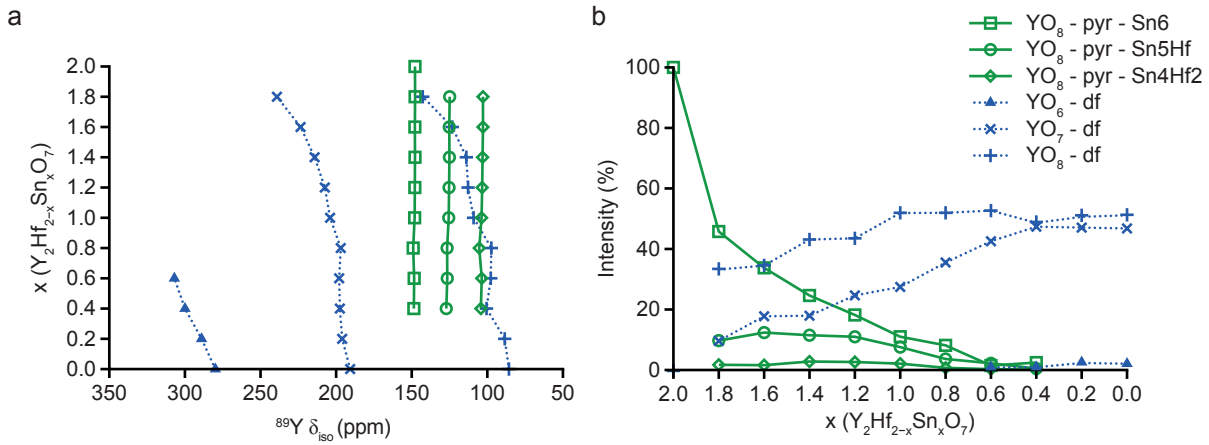

Figure S4.2. Plot showing the variation of (a) chemical shifts and (b) integrated intensities of resonances in the ^{89}Y MAS NMR spectra of $Y_2Hf_{2-x}Sn_xO_7$ with nominal composition. Resonances attributed to the pyrochlore and defect fluorite phases are denoted pyr and df, respectively. For the pyrochlore phase, the B site NNN arrangement for each environment is also shown.

S5. Further information on ^{119}Sn MAS NMR spectra

Figure S5.1 shows the result of the analytical fitting of ^{119}Sn MAS NMR spectra of $Y_2Hf_{0.2}Sn_{1.8}O_7$.

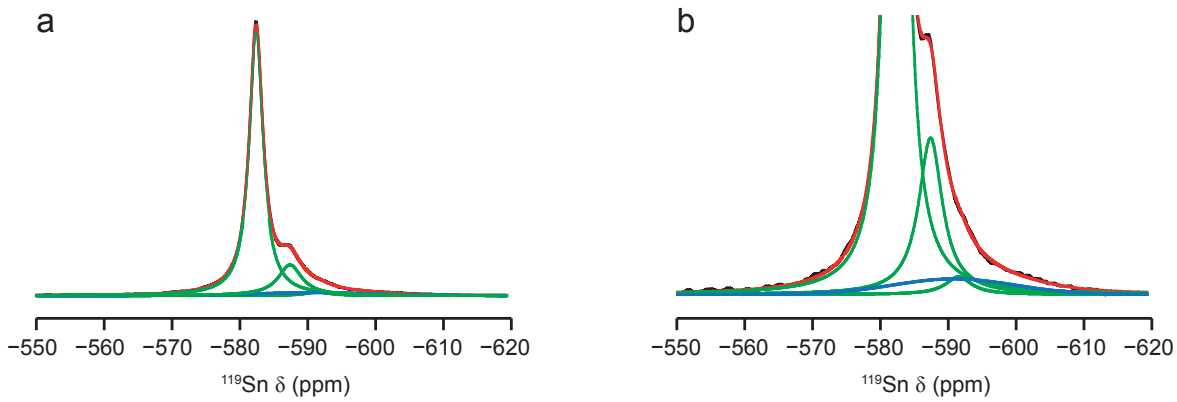

Figure S5.1. (a) Analytical fit and (b) corresponding (vertical) expansion of the ^{119}Sn MAS NMR spectrum of $Y_2Hf_{0.2}Sn_{1.8}O_7$. The green, blue and red lines denote the analytical fit for the pyrochlore phase, defect fluorite phase and all resonances, respectively.

From a fitting of each of the ^{119}Sn MAS NMR spectra of $Y_2Hf_{2-x}Sn_xO_7$ in Figure 5 of the main text, the chemical shifts of the individual components, and their relative intensities can be extracted. These are given in Table 2 (main text) and shown in Figure S5.2 as a function of the composition of the starting materials.

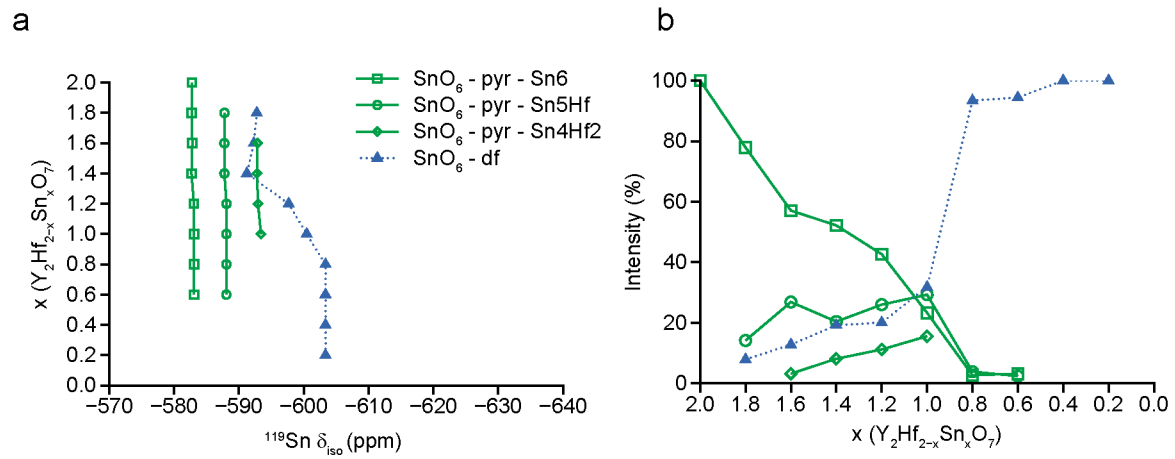

Figure S5.2. Plot showing the variation of (a) chemical shifts and (b) integrated intensities of resonances in the ^{119}Sn MAS NMR spectra of $Y_2Hf_{2-x}Sn_xO_7$ with nominal composition. Resonances attributed to the pyrochlore and defect fluorite phases are denoted pyr and df, respectively. For the pyrochlore phase, the B site NNN arrangement for each environment is also shown.

All of the resonances in the ^{119}Sn NMR spectra in Figure 5 have chemical shifts commonly associated with six-coordinate Sn species, suggesting not only that Sn is confined to the B site in the pyrochlore phase, but that it also adopts six-fold coordination in the disordered defect fluorite phase, *i.e.*, that the vacancies are preferentially associated with Sn over Y or Hf. Figure S5.3 confirms that no signal is seen at shifts corresponding to higher (*i.e.*, seven- and eight-coordinate) Sn species in the ^{119}Sn MAS NMR spectrum of $Y_2Hf_{1.8}Sn_{0.2}O_7$ acquired using a wider spectral width. Here calculated ^{119}Sn δ_{iso} for pyrochlore models of $Y_2Sn_2O_7$ against where oxygen atoms have been moved from 8a to vacant 8b sites thereby changing the Sn coordination number are also shown (as in Figure 6b of the main text).

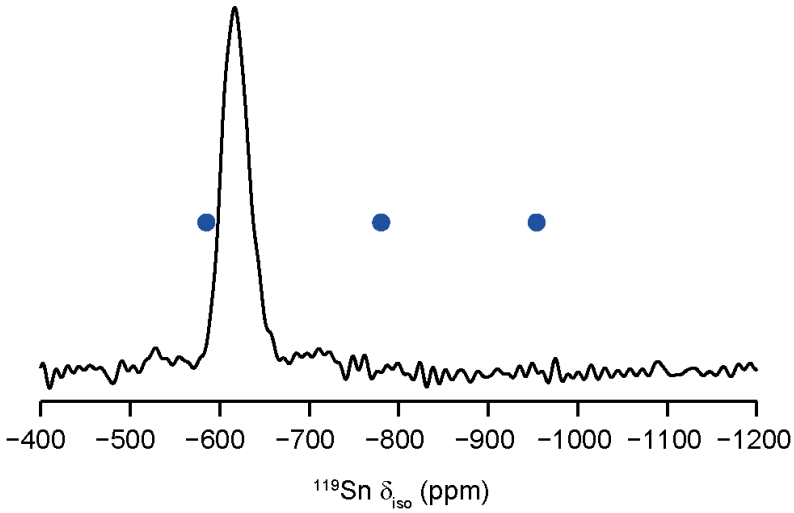

Figure S5.3. ^{119}Sn (9.4 T, 14 kHz) MAS NMR spectrum of $Y_2Hf_{1.8}Sn_{0.2}O_7$, acquired using a spin echo sequence. The blue dots represent calculated ^{119}Sn δ_{iso} for pyrochlore models with six-, seven- and eight-coordinated Sn, as in Figure 6b of the main text.

S6. Further information on ^{17}O MAS NMR spectra

Figure S6.1 shows ^{17}O MAS NMR spectra of a 1 : 1 molar physical mixture of $Y_2Sn_2O_7$ and $Y_2Hf_2O_7$, enriched at two different temperatures. The spectra have been normalised to the intensity of the defect fluorite peak at ~310 ppm. It is clear that at lower temperature the relative level of enrichment of the two phases is different, with preferential enrichment of the defect fluorite ($Y_2Hf_2O_7$) phase. At the higher temperature, the relative intensities of the signals from the pyrochlore and defect fluorite signals are 0.65 : 1.35, not the 1 : 1 that might be expected. As discussed in Ref. S9, there are no differences in nutation of the different signals at the short flip angles used. However, when spectra were acquired with a much longer recycle interval (1500 s), an increase in the intensity of the pyrochlore signals (of 3.35 and 2.2, for O1 and O2, respectively) was observed. For signals with very low C_Q (*i.e.*, O1 in the pyrochlore phase and all signals in the defect fluorite phase), it is also necessary to take into account the contribution of the satellite transitions (ST) to the spectral intensities (see Ref. S9 for further information). Once these corrections (factors of 3.89 for pyrochlore O1 and 1.08 for defect fluorite signals), the relative intensities of the signals from the two phases are 1 : 1, as expected. This demonstrates that uniform relative enrichment of both phases is obtained with enrichment at 900 °C for 12 h.

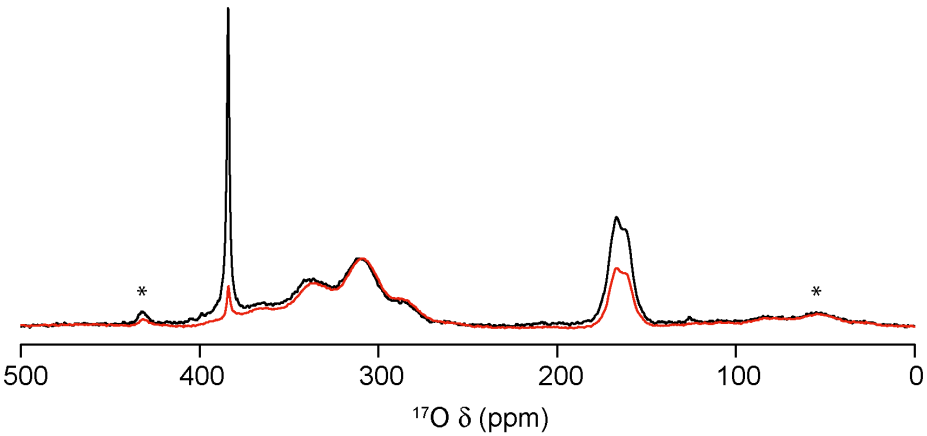

Figure S6.1. ^{17}O (14.1 T, 21 kHz) MAS NMR spectrum of a molar 1 : 1 physical mixture of $Y_2Sn_2O_7$ and $Y_2Hf_2O_7$ enriched at 600 °C (red) and 900 °C (black) for 12 h. The spectra were acquired using a recycle interval of 5 s. Spinning sidebands are marked with *.

Figure S6.3 shows expansions of the ^{17}O (MAS NMR spectra of $Y_2Hf_{2-x}Sn_xO_7$ with x = 1.8, 1.6 and 1.2, confirming the presence of resonances from a defect fluorite phase even at low Hf compositions.

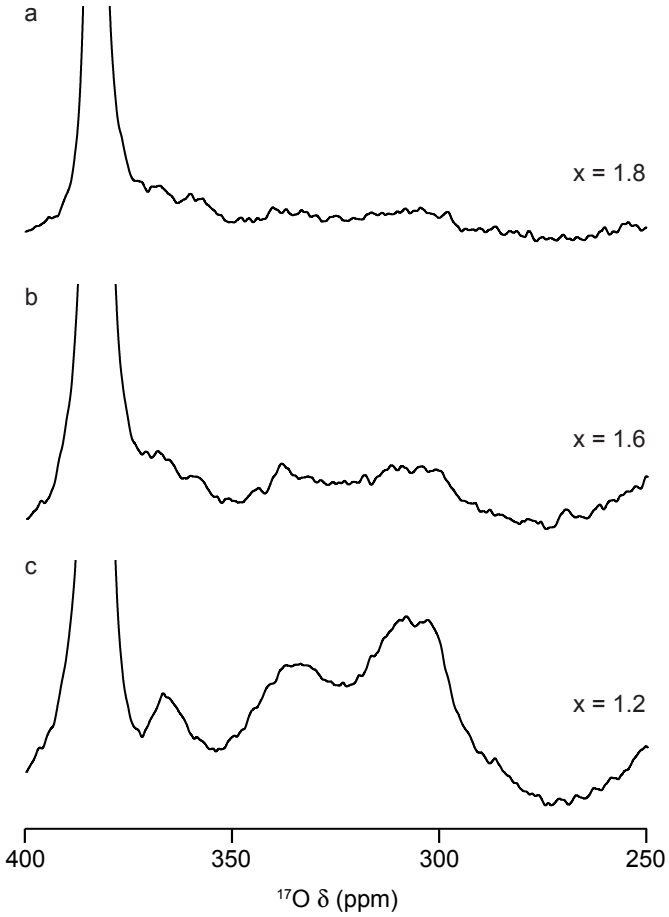

Figure S6.2. Expansions of ^{17}O (14.1 T, 21 kHz) MAS NMR spectra of $Y_2Hf_{2-x}Sn_xO_7$, enriched at 900 °C for 12 h, with x = (a) 1.8, (b) 1.6 and (c) 1.2.

Figure S6.3 shows a ^{17}O MQMAS NMR spectrum of $Y_2Sn_{0.6}Hf_{1.4}O_7$ (expanded to show the region corresponding to OX3Sn) enriched 900 °C for 12 h. The spectrum was acquired using a z-filtered pulse sequence but is shown after shearing, with the δ_1 axis referenced according to the convention in Ref. S14. From the position of the centre-of-gravity of the lineshape values of $\langle\delta_{iso}\rangle \approx$ ~238 ppm and $\langle P_Q\rangle \approx$ ~2.6 MHz can be extracted, demonstrating the broadening observed in the MAS spectrum arises primarily from a distribution of chemical shifts.

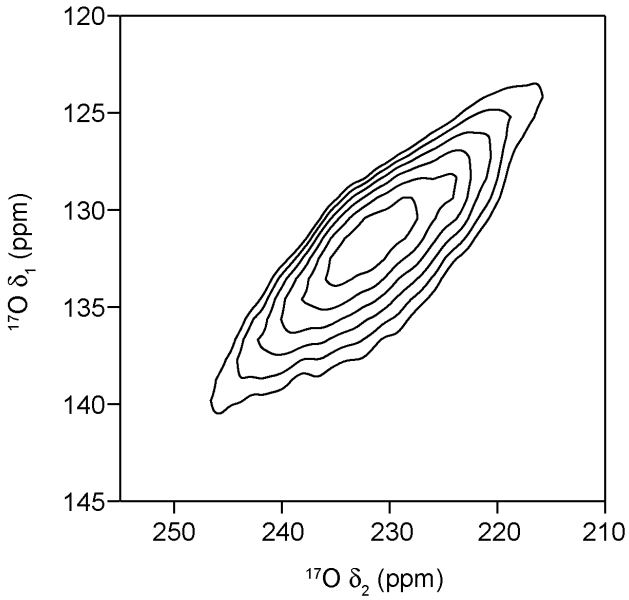

Figure S6.3. ^{17}O (14.1 T, 21 kHz) MQMAS NMR spectrum of $Y_2Sn_{0.6}Hf_{1.4}O_7$ (expanded to show the region corresponding to OX3Sn) enriched 900 °C for 12 h.

S7. Comparison of average coordination numbers in defect fluorite phases

Figure S7.1 compares the variation in average coordination number of Y, Sn and Hf/Zr in $Y_2(Hf,Sn)_2O_7$ and $Y_2(Zr,Sn)_2O_7$ disordered defect fluorite phases as a function of composition. Values for $Y_2(Zr,Sn)_2O_7$ have been taken from Ref. S15.

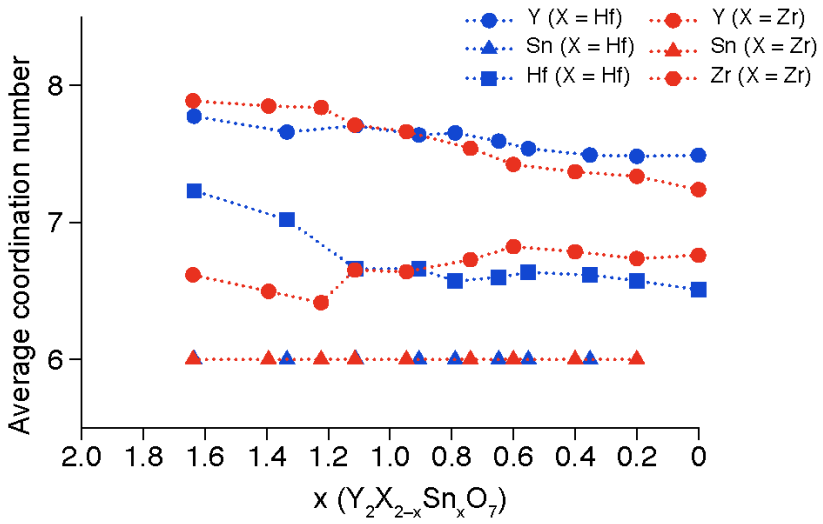

Figure S7.1. Plot showing the variation in average coordination number of Y, Sn and Hf/Zr in disordered defect fluorite $Y_2X_{2-x}Sn_xO_7$ (where X = H or Zr) as a function of the actual (not nominal) composition.

S8. References

S1. Pickard, C. J.; Mauri, F. All-Electron Magnetic Response with Pseudopotentials: NMR Chemical Shifts. *Phys. Rev. B: Condens. Matter Mater. Phys*. **2001**, *63*, 245101.

S2. Clark, S. J.; Segall, M. D.; Pickard, C. J.; Hasnip, P. J.; Probert, M. J.; Refson, K.; Payne, M. C. First-Principles Methods using CASTEP. *Z. Kristallogr. - Cryst. Mater.* **2005**, *220*, 567-570.

S3. Perdew, J. P.; Burke, K.; Ernzerhof, M. Generalized Gradient Approximation Made Simple. *Phys. Rev. Lett.* **1996**, *77*, 1865-1868.

S4. Vanderbilt, D. Soft Self-Consistent Pseudopotentials in a Generalized Eigenvalue Formalism. *Phys. Rev. B: Condens. Matter Mater. Phys*. **1990**, *41*, 7892-7895.

S5. Yates, J. R.; Pickard, C. J.; Payne, M. C.; Mauri, F. Relativistic Nuclear Magnetic Resonance Chemical Shifts of Heavy Nuclei with Pseudopotentials and the Zeroth-Order Regular Approximation. *J. Chem. Phys*. **2003**, *118*, 5746-5743.

S6. Monkhorst, H. J.; Pack, J. D. Special Points for Brillouin-Zone Integrations. *Phys. Rev. B* **1976**, *13*, 5188-5192.

38. Pyykko, P., Year-2017 Nuclear Quadrupole Moments. *Mol. Phys.* **2018,** *116*, 1328-1338.

S7. Moran, R. F. Investigating the use of First-Principles Calculations for NMR Studies in the Solid State. PhD Thesis, University of St Andrews, **2019**.

S8. Grey, C. P.; Dobson, C. M.; Cheetham, A. K.; Jakeman, R. J. B. Studies of Rare-Earth Stannates by ^{119}Sn MAS NMR. The Use of Paramagnetic Shift Probes in the Solid State. *J. Am. Chem. Soc*. **1989**, *111*, 505-511.

S9. Fernandes, A.; Moran, R. F.; Sneddon, S.; Dawson, D. M.; McKay, D.; Bignami, G. P. M.; Blanc, F.; Whittle, K. R.; Ashbrook S. E. ^{17}O Solid-State NMR Spectroscopy of $A_2B_2O_7$ Oxides: Quantitative Isotopic Enrichment and Spectral Acquisition? *RSC Adv*. **2018**, *8*, 7089-7101.

S10. Orr, R. M.; Duer, M. J.; Ashbrook, S. E. Correlating Fast and Slow Chemical Shift Spinning Sideband Patterns in Solid-State NMR. *J. Magn. Reson*. **2005**, *174*, 301-309.

S11. Orr, R. M.; Duer, M. J. Applications of the CSA-Amplified PASS Experiment. *Solid State Nucl. Magn. Reson*. **2006**, *30*, 1-8.

S12. Levitt, M. H.; Madhu, P. K.; Hughes, C. E. Cogwheel Phase Cycling. *J. Magn. Reson.* **2002**, *155*, 300-306.

S13. Bak, M.; Rasmussen, J.; Nielsen, N. SIMPSON: a General Simulation Program for Solid-State NMR Spectroscopy. *J. Magn. Reson*. **2000**, *147*, 296-330.

S14. Pike, K. J.; Malde, R. P.; Ashbrook, S. E.; McManus, J.; Wimperis, S. Multiple-Quantum MAS NMR of Quadrupolar Nuclei. Do Five-, Seven- and Nine-Quantum Experiments Yield Higher Resolution than the Three-Quantum Experiment? *Solid State Nucl. Magn. Reson*. **2000**, *16*, 203-215.

S15. Ashbrook, S. E.; Mitchell, M. R.; Sneddon, S.; Moran, R. F.; de los Reyes, M.; Lumpkin G. R.; Whittle, K. R. New Insights into Phase Distribution, Phase Composition and Disorder in $Y_2(Zr,Sn)_2O_7$ Ceramics from NMR Spectroscopy. *Phys. Chem. Chem. Phys*. **2015**, *17*, 9049-9059.